Progress In Electromagnetics Research, Vol. 173, 129–140, 2022

A Physics-Based HIE-FDTD Method for Electromagnetic Modeling of Multi-Band Frequency Selective Surface

Hao Xie[1, 2], Tielun Hu[2], Zhili Wang[3], Yanbin Yang[4], Xiaohui Hu[1], Wei Qi[1], and Hong Liu[1, *]

(*Invited*)

Abstract—A physics-based hybrid implicit-explicit finite-difference time domain (HIE-FDTD) method is developed for electromagnetic modeling of multi-passband frequency selective surfaces (FSSs). Using this self-developed HIE-FDTD simulator, several dual- and tri-passband FSSs are designed and further fabricated. The measurement results are in good agreement with the simulation ones, which prove high accuracy of the self-developed HIE-FDTD algorithm. In addition, the resonant frequencies of the designed FSSs can be effectively adjusted by changing their geometric parameters. This work provides electromagnetic guides of structure and parameter selections for designing multi-passband FSS.

1. INTRODUCTION

Frequency selective surface (FSS), as a spatial filter, is a planar periodic structure with filtering characteristics for electromagnetic waves [1]. It is critical for applications of satellite communication technology, electromagnetic radiation environment and protection, which can protect the antenna system from high-power microwave (HPM) [2]. With the increasing demand of FSS applications, single band FSS no longer meets the requirement. Recently, multi-band FSS has attracted a lot of attention in communication system because of its several independent operating frequency ranges characteristics [1–6]. The common structural design methods of multi-band FSS are as follows: stack multi-resonant element [7–10], perturbations of a single-band element [11–13], fractal element [14, 15], and three-dimensional composite topology element [16]. The frequency adjustability by the parameters of the multi-band FSS needs to be further studied due to the urgent need of its various operation frequency ranges in communication system.

The main methods used in FSS numerical simulation are full spectrum domain method [17], finite-difference time domain (FDTD) algorithm [18–21], finite element domain (FEM) algorithm [22, 23], etc. Among these methods, FDTD has been widely used because of its accurate description about the transmission characteristics of FSS [18]. However, the traditional FDTD method with periodic boundary condition requires large memory resources and long simulation time. Therefore, hybrid implicit-explicit finite-difference time domain (HIE-FDTD) method has been developed to solve such electromagnetic problems with fine grid in one direction but rough grids in the other two directions [24, 25]. It is more suitable for computing large scale finite FSS arrays as compared with the traditional FDTD [24–27].

Received 21 January 2022, Accepted 8 April 2022, Scheduled 20 April 2022

* Corresponding author: Hong Liu (liuhong@zucc.edu.cn).

[1] School of Information and Electrical Engineering, Zhejiang University City College, Hangzhou 310015, China. [2] Innovative Institute of Electromagnetic Information and Electronic Integration (EIEI), College of Information Science and Electronic Engineering, Zhejiang University, Hangzhou 310027, China. [3] Science and Technology on Electromagnetic Compatibility Laboratory, China Ship Development and Design Centre, Wuhan 430064, China. [4] Zhijiang Intelligence Institute in Chengdu Tianfu District, Chengdu 610213, China.

This paper is organized as follows. The HIE-FDTD formula is derived and presented in Section 2. In Section 3, several multi-passband FSSs are designed and further fabricated. The comparison between simulated and experimental results shows that the HIE-FDTD method has good computational accuracy. Besides, the transmission coefficients of the FSSs can be effectively adjusted by changing their geometric parameters. Conclusions are drawn in Section 4.

2. FORMULATION AND MODEL

2.1. HIE-FDTD Method

HIE-FDTD method is more suitable for solving electromagnetic problems with fine grid in one direction but coarse grids in the other two directions [24, 25]. Because of its explicit difference iteration in two directions and implicit difference iteration in the remaining one, its time step is limited only by the maximum two spatial steps. Therefore, its computational efficiency is much higher than the traditional FDTD, since the time step of HIE-FDTD can be much larger.

The fine grid is set in the y-direction with respect to the coordinate system, and the HIE-FDTD equations can be given as follows [19].

$$E_y^{n+1/2} = E_y^{n-1/2} + \frac{\Delta t}{\varepsilon \Delta z}\left(H_x^n - H_{x,k-1}^n\right) - \frac{\Delta t}{\varepsilon \Delta x}\left(H_z^n - H_{z,i-1}^n\right) \tag{1}$$

$$H_y^{n+1/2} = H_y^{n-1/2} + \frac{\Delta t}{\mu \Delta x}\left(E_{z,i+1}^n - E_z^n\right) - \frac{\Delta t}{\mu \Delta z}\left(E_{x,k+1}^n - E_x^n\right) \tag{2}$$

$$E_x^{n+1} = E_x^n - \frac{\Delta t}{\varepsilon \Delta z}\left(H_y^{n+1/2} - H_{y,k-1}^{n+1/2}\right) + \frac{\Delta t}{2\varepsilon \Delta y}\left(H_z^{n+1} - H_{z,j-1}^{n+1} + H_z^n - H_{z,j-1}^n\right) \tag{3}$$

$$E_z^{n+1} = E_z^n + \frac{\Delta t}{\varepsilon \Delta x}\left(H_y^{n+1/2} - H_{y,i-1}^{n+1/2}\right) + \frac{\Delta t}{2\varepsilon \Delta y}\left(H_x^{n+1} - H_{x,j-1}^{n+1} + H_x^n - H_{x,j-1}^n\right) \tag{4}$$

$$H_z^{n+1} = H_z^n - \frac{\Delta t}{\mu \Delta x}\left(E_{y,i+1}^{n+1/2} - E_y^{n+1/2}\right) + \frac{\Delta t}{2\mu \Delta y}\left(E_{x,j+1}^{n+1} - E_x^{n+1} + E_{x,j+1}^n - E_x^n\right) \tag{5}$$

$$H_x^{n+1} = H_x^n + \frac{\Delta t}{\mu \Delta z}\left(E_{y,k+1}^{n+1/2} - E_y^{n+1/2}\right) - \frac{\Delta t}{2\mu \Delta y}\left(E_{z,j+1}^{n+1} - E_z^{n+1} + E_{z,j+1}^n - E_z^n\right) \tag{6}$$

It can be seen that Eqs. (3) and (4) contain unknown variables, which require implicit iteration. In order to eliminate the unknown variable H_z^{n+1}, the iteration equation of E_x-component can be obtained by substituting Eq. (5) into Eq. (3).

$$\begin{aligned}
&\left(1 + \frac{(\Delta t)^2}{2\mu\varepsilon(\Delta y)^2}\right) E_x^{n+1} - \frac{(\Delta t)^2}{4\mu\varepsilon(\Delta y)^2}\left(E_{x,j-1}^{n+1} + E_{x,j+1}^{n+1}\right) \\
&= \left(1 - \frac{(\Delta t)^2}{2\mu\varepsilon(\Delta y)^2}\right) E_x^n + \frac{(\Delta t)^2}{4\mu\varepsilon(\Delta y)^2}\left(E_{x,j-1}^n + E_{x,j+1}^n\right) \\
&\quad + \frac{\Delta t}{\varepsilon \Delta y}\left(H_z^n - H_{z,j-1}^n\right) - \frac{\Delta t}{\varepsilon \Delta z}\left(H_y^{n+\frac{1}{2}} - H_{y,k-1}^{n+\frac{1}{2}}\right) \\
&\quad - \frac{(\Delta t)^2}{2\mu\varepsilon \Delta x \Delta y}\left(E_{y,i+1}^{n+1/2} - E_y^{n+1/2} - E_{y,i+1,j-1}^{n+1/2} + E_{y,j-1}^{n+1/2}\right)
\end{aligned} \tag{7}$$

Similarly, in order to eliminate H_x^{n+1}, we substitute Eq. (6) into Eq. (4), and the iteration equation of E_z-component is given by

$$\begin{aligned}
&\left(1 + \frac{(\Delta t)^2}{2\mu\varepsilon(\Delta y)^2}\right) E_z^{n+1} - \frac{(\Delta t)^2}{4\mu\varepsilon(\Delta y)^2}\left(E_{z,j-1}^{n+1} + E_{z,j+1}^{n+1}\right) \\
&= \left(1 - \frac{(\Delta t)^2}{2\mu\varepsilon(\Delta y)^2}\right) E_z^n + \frac{(\Delta t)^2}{4\mu\varepsilon(\Delta y)^2}\left(E_{z,j-1}^n + E_{z,j+1}^n\right)
\end{aligned}$$

$$+\frac{\Delta t}{\varepsilon \Delta x}\left(H_y^{n+\frac{1}{2}} - H_{y,i-1}^{n+\frac{1}{2}}\right) - \frac{\Delta t}{\varepsilon \Delta y}\left(H_x^n - H_{x,j-1}^n\right)$$
$$-\frac{(\Delta t)^2}{2\mu\varepsilon \Delta z \Delta y}\left(E_{y,k+1}^{n+1/2} - E_y^{n+1/2} - E_{y,j-1,k+1}^{n+1/2} + E_{y,j-1}^{n+1/2}\right) \tag{8}$$

At the same time, H_z^{n+1} and H_x^{n+1} can be obtained directly by an explicit iteration according to Eqs. (5) and (6).

In order to ensure the stability of electromagnetic field components in iterations, the magnitude of growth factor should not be greater than 1. Therefore, the time step of HIE-FDTD satisfies the following conditions [19],

$$\Delta t \leq \frac{1}{c\sqrt{\Delta x^{-2} + \Delta z^{-2}}} \tag{9}$$

From Eq. (9), the preferable Δt may be many times larger than that of normal FDTD when dealing with problems of fine spatial cell.

2.2. Simulation Model

Figure 1 is the schematic diagram of the FSS array which is placed in the x-z plane, while the incident plane wave is in z-polarization. The periodic boundary conditions (PBCs) in x- and z-directions are applied to simulate FSS array. Incident plane waves are introduced into the total field/scattering field (TF/SF) boundary. Convolution perfectly matched layer (CPML) is used to truncate the open space in the y-direction.

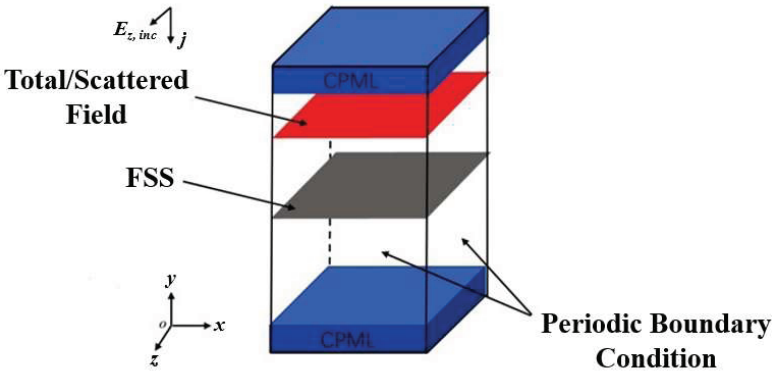

Figure 1. A plane wave normally incident on an FSS array.

A TF/SF boundary is used to introduce an incident plane wave described by,

$$E = \sin\left(2\pi * f_0\left(n * dt - 3 * delay * dt\right)\right) * \exp\left(-\left(\frac{n}{delay} - 3\right)^2\right) \tag{10}$$

where f_0 is the frequency, dt the time step, n the number of time steps, and $delay$ the time delay, which is defined as,

$$delay = 1/cband/dt \tag{11}$$

where $cband$ is the signal bandwidth.

Since it is difficult to apply periodic boundary in time domain when incident wave is obliquely incident, this problem is solved in frequency domain. Reference [28] introduces the application of periodic boundary conditions when modulated Gaussian pulse wave is obliquely incident. At this time, the incident wave is called complex sinusoidal modulated Gaussian pulse, which is given by,

$$E_i(x, y, z, t) = F(x, y, z)\left(\cos\omega t + j\sin\omega t\right)\exp\left[-\frac{(t - t_0)^2}{T^2}\right] \tag{12}$$

where t is the time, t_0 the start-up delay, T the period of the incident wave, and $F(x, y, z)$ the spatial variation of incident wave amplitude, which is corresponding to the fundamental incident wave propagation mode.

3. NUMERICAL RESULTS AND DISCUSSION

In order to meet the performance requirements of multi-passbands at different frequencies, many kinds of FSSs of cross grove and fork FSS structures with different geometric parameters are designed by the self-developed physics-based HIE-FDTD method. Based on cross grove and fork FSS structures, the resonant frequencies of the designed FSSs can be effectively adjusted by changing their geometric parameters.

3.1. Cross Grove FSS Structure

The self-similarity method is used to design the dual-passband FSS, which can be understood as that there are two or more structures with the same geometry but different sizes in a structure, where the smaller structures are often included in the larger structures [14, 29]. Fig. 2 shows the structural sketch of dual-passband FSS unit, in which a smaller cross groove is contained in the larger one. The length and width of the big(small) cross groove are represented by $W_{1(2)}$, and $L_{1(2)}$, respectively. The parameters of g_1 and g_2 are the gap widths of big and small cross grooves, respectively. The two cross grooves with different sizes have different resonant frequencies, which can achieve the dual-passband characteristics of FSS. The resonant frequency can be adjusted by changing the sizes of W_1, W_2, L_1, and L_2, while the plane symmetry of the structure about x-y and z-y remains unchanged. However, changing the parameter of W will alter the distance between the two cross grooves and introduce a strong coupling effect, so the distance s between the cross grooves should not be too small.

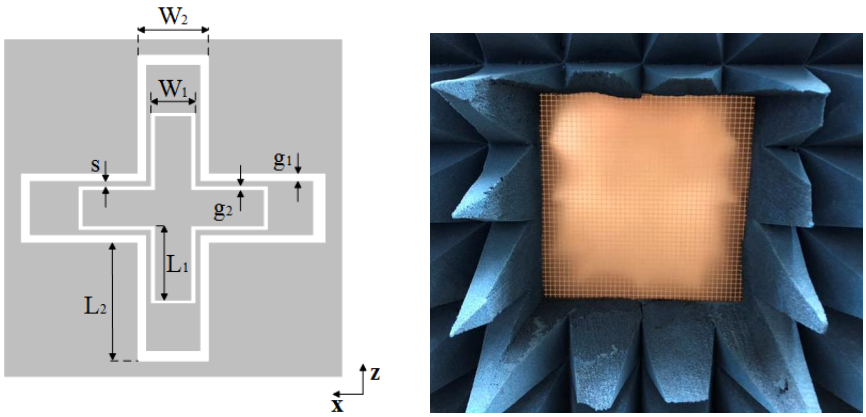

Figure 2. (a) Structural sketch of dual-passband FSS unit, and (b) manufactured FSS sample.

According to the requirements of relevant applications, three kinds of dual-passband FSSs of C and X bands, X and Ku bands, and C and Ku bands are designed by changing the parameters of FSS unit, and their parameters are indicated in Table 1. The FSSs are further fabricated by the metal material of Cu and dielectric substrates of F4BM-220 as shown in Fig. 2(b). The FSS array is placed on dielectric substrates with the thickness of 0.5 mm, relative dielectric constant of 2.2, and loss tangent of 7×10^{-4}.

The designed FSSs are manufactured, and their performances and the accuracy of simulations are further tested. Fig. 3 shows the schematic diagram of measurement system of FSS. In experiment, the transmitting and receiving horns are ultra-wideband ridged horns with operating frequency range of 2 GHz–18 GHz. From calculation, the minimum test distance between the FSS and transmitting horn should be greater than 1 m. A low noise amplifier is connected to the receiving horn, which is also

Table 1. Parameters of FSS samples (unit: mm).

Symbols	L_1	L_2	W_1	W_2	g_1	g_2	s
FSS sample of Fig. 4	5	3	2.4	1.2	0.2	0.2	0.4
FSS sample of Fig. 5	2.7	2.2	1.2	0.6	0.2	0.2	0.1
FSS sample of Fig. 6	4.2	1.8	2	1	0.2	0.2	0.3

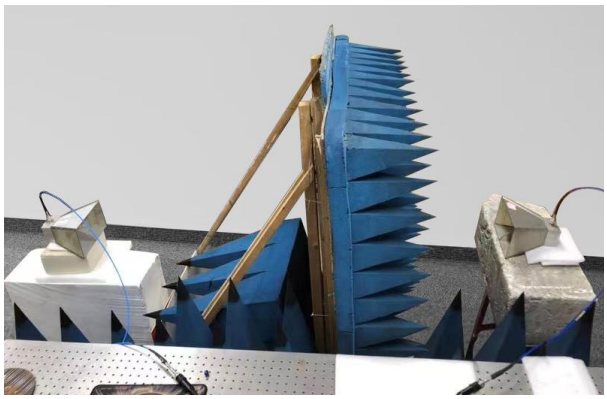

Figure 3. Schematic diagram of measurement system.

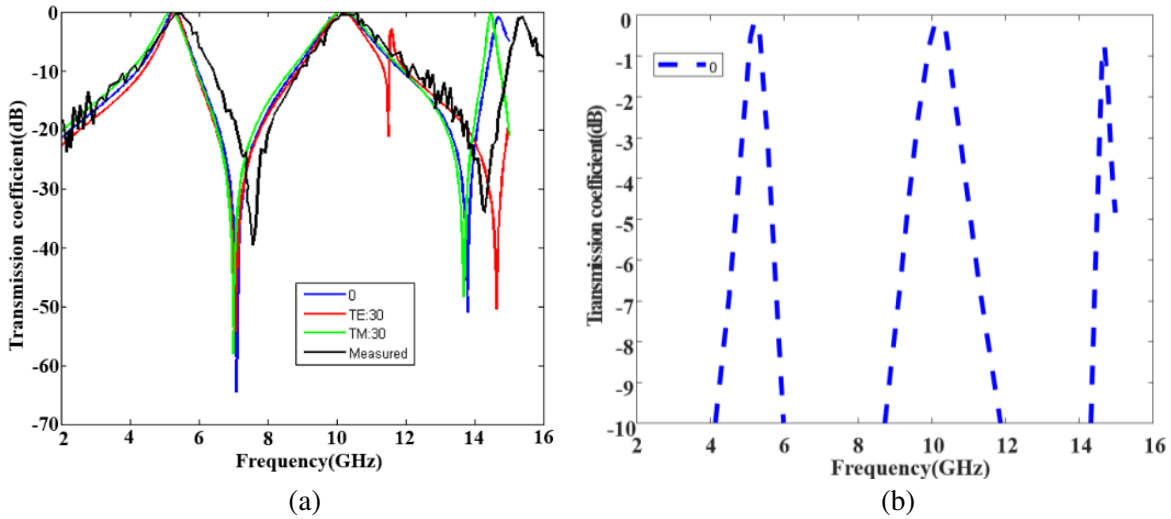

Figure 4. Transmission coefficient in simulation and experiment of C and X band FSSs with different vertical scales: (a) -70 to 0 dB, and (b) -10 to 0 dB.

connected to the input port of the vector network analyzer. The transmitting horn is connected to the output port of the vector network analyzer, and FSS sample is surrounded by absorbing materials.

Figure 4 shows transmission coefficient in HIE-FDTD simulation and experiment of C and X passband FSSs. The FSS sample contains 40×40 FSS units, in which the sample size is $0.55\,\text{m} \times 0.55\,\text{m}$, and the array period is 13.2 mm.

It can be seen that the resonant frequencies are 5.3 GHz and 10.1 GHz, and the HIE-FDTD simulated and experimental results are in good agreement. The bandwidths of the simulated and experimental results are also relatively close. In addition, the resonant frequency and bandwidth of FSS

are basically unchanged while the incident angle is small. The gate lobe effect is observed at higher frequency in both experimental and simulated results.

A dual-passband FSS design of X and Ku bands is further completed by adjusting the relevant dimensions, and the resonant frequencies of simulation are 9.7 GHz and 15.9 GHz. The manufactured FSS sample contains 60×60 FSS units, in which the sample size is $0.45\,\text{m} \times 0.45\,\text{m}$, and the array period is 7 mm. The parameters of dielectric substrates remain unchanged.

Figure 5 shows the transmission coefficient in HIE-FDTD simulation and experiment of X and Ku passband FSSs. The experimental and HIE-FDTD simulation results agree well, but the resonant frequency of the first passband is offset by 0.5 GHz.

In order to get the dual-passband FSS design in C and Ku bands, an FSS with resonant frequencies of 6.4 GHz and 14.9 GHz is designed by further adjusting the relevant parameters. The FSS sample contains 40×40 FSS units, in which the sample size is $0.45\,\text{m} \times 0.45\,\text{m}$, and the array period is 11 mm. The HIE-FDTD simulation and test results are shown in Fig. 6, which are also in good agreement. The

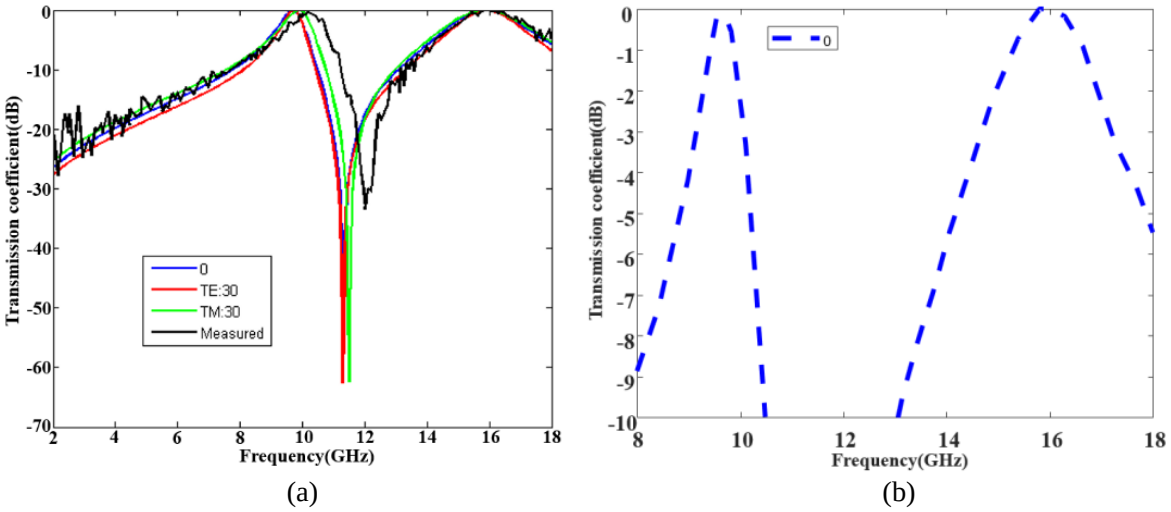

Figure 5. Transmission coefficient in simulation and experiment of X and Ku band FSSs with different vertical scales: (a) −70 to 0 dB, and (b) −10 to 0 dB.

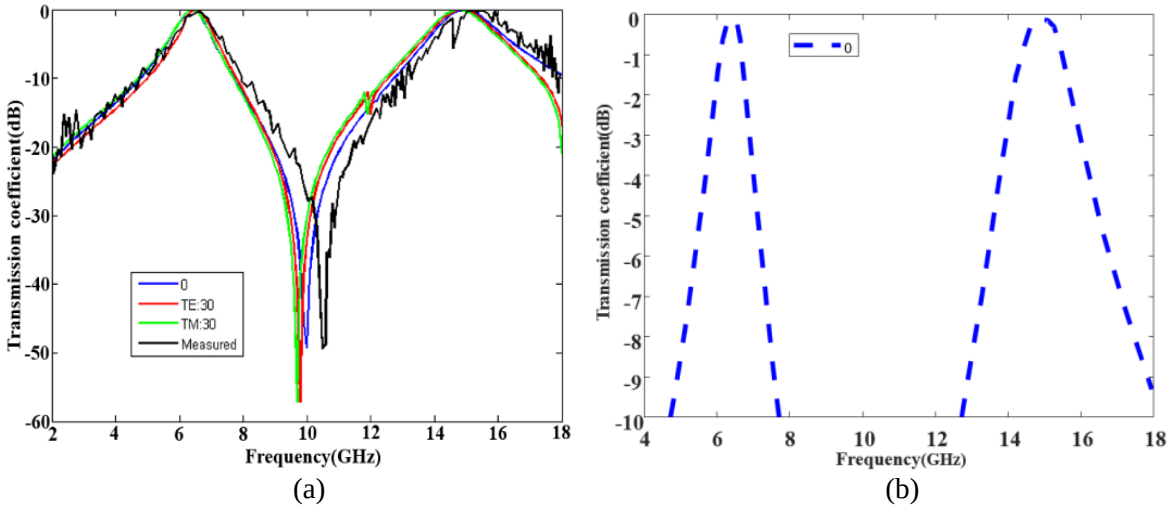

Figure 6. Transmission coefficient in simulation and experiment of C and Ku band FSSs with different vertical scales: (a) −60 to 0 dB, and (b) −10 to 0 dB.

resonant frequencies of the first passband of the simulation and test values are almost the same, but there is a frequency shift of 0.4 GHz of the second passband.

The proposed structure has good resonance frequency point stability characteristics, and the frequency shift of resonance frequency point is stable within 0.5 GHz at different angles of incidence. The bandwidth changes obviously with different incident angles and polarization states.

3.2. Fork FSS Structure

The multi-passband metallic fork FSS with wide range of band ratio has been proposed in [30]. The FSS structure is based on a single metal layer without a dielectric layer, which can achieve multi-passband characteristics. Fig. 7 shows the structural sketch of multi-passband FSS unit. The gray part is metal of Cu, and white part is air. The FSS unit has four square slots, and each contains multiple ($n = 3$, 4) resonant units. In order to reduce the unit size, each resonance element in the square is changed from Fig. 7(c) to Fig. 7(d). Fig. 7(b) shows the structural parameters of the resonance elements in each square slot.

Based on the high pass characteristic of the square slot, the resonant unit is introduced into the square slot to realize the band-pass response. Multi-passbands can be realized because several units

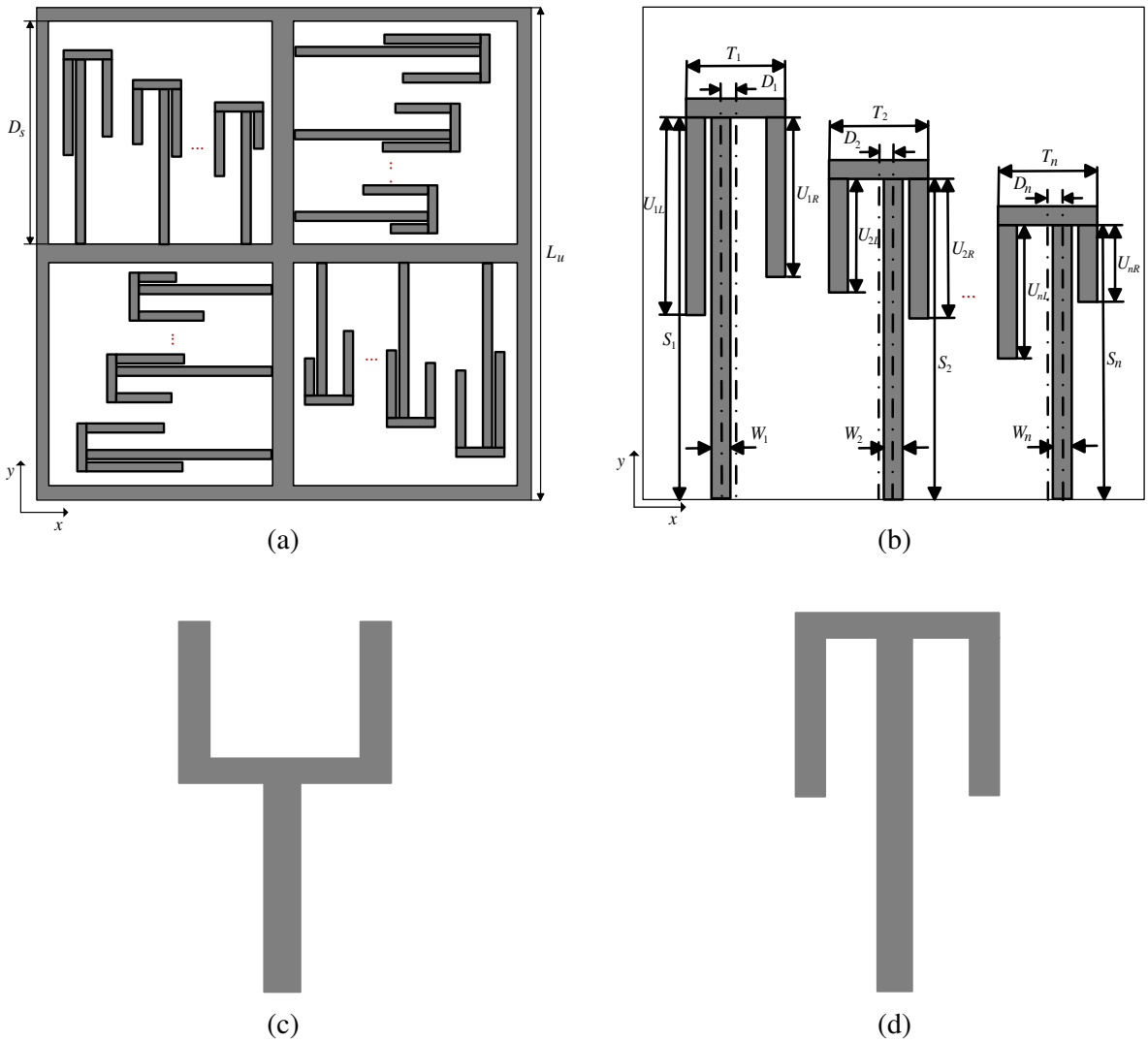

Figure 7. (a) Structural sketch of triple-passband FSS unit, (b) unit size, (c) basic resonant element, and (d) variations of basic resonant element.

have different resonant frequencies. By using the rotation-invariant property of the special arrangement of four square slots, the structure can achieve response stability while the wave irradiates at different polarizations and incident angles. Since the four square slots are arranged with rotation invariant characteristics, they are insensitive to TE and TM polarized waves and have similar frequency response characteristics. In addition, this structure has an advantage that the resonant frequency of each passband corresponds to the resonant unit in a square groove. Therefore, the central frequency of each passband can be adjusted by changing the size of the corresponding resonant unit.

Figure 8 shows the equivalent lumped element circuit model of FSS unit mentioned above, where *Ls* influence the high-pass characteristic of square slot, and the equivalent circuit loaded in the square is a *LC* resonator in parallel to the *Ls*. Each *LC* resonant unit corresponds to a resonant unit in a square slot, similar to a bandpass filter.

According to the requirements of relevant applications, four kinds of multi-passband FSSs are realized by changing the parameters of FSS unit. The central frequency of specific passband varies with the size of the corresponding resonant unit change. Fig. 9 shows the transmission coefficient of dual-passband FSS with different lengths of U_2 by HIE-FDTD simulation. The first resonant unit corresponds to the passband with lower frequency, and the passband with higher resonant frequency corresponds to the second resonant unit. While adjusting the size of the second resonant unit, the center frequency of

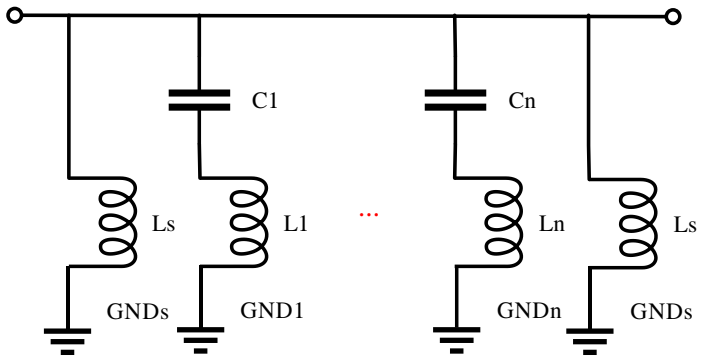

Figure 8. Equivalent lumped element circuit model.

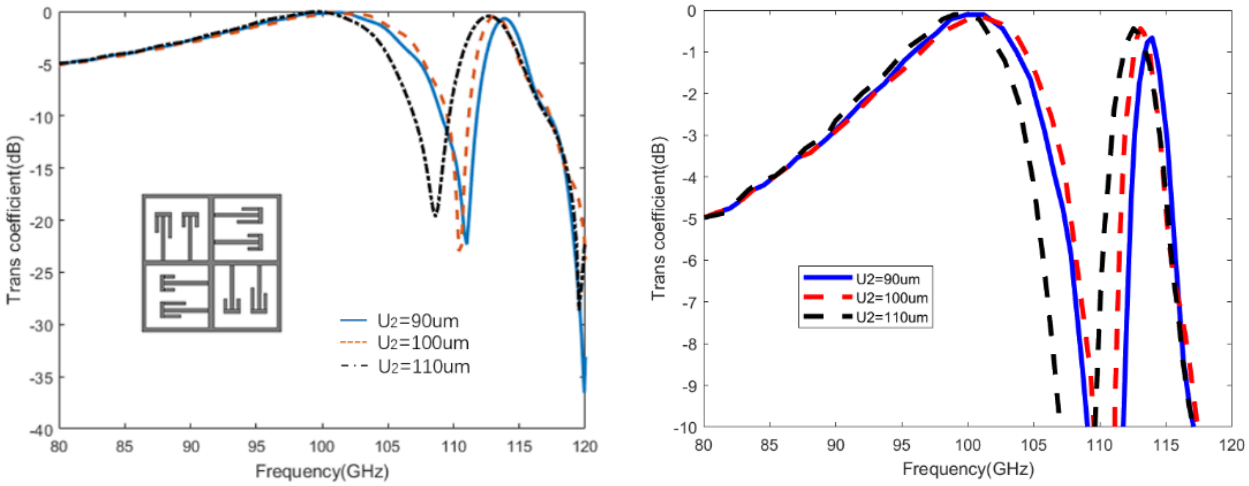

Figure 9. Transmission coefficient of dual-passband FSS with different length of U_2 with different vertical scales: (a) −40 to 0 dB, and (b) −10 to 0 dB ($L_u = 1220\,\mu m$, $D_s = 530\,\mu m$, $T_1 = T_2 = 150\,\mu m$, $S_1 = S_2 = 350\,\mu m$, $U_1 = 200\,\mu m$, $W_1 = W_2 = 30\,\mu m$).

the first resonant unit is almost unchanged. However, the center frequencies of the second passband are 112.5 GHz, 112.8 GHz, and 113.6 GHz, respectively. It is indicated that each passband corresponds to a resonant unit, i.e., each passband is independent. In addition, the resonant frequency of the cell will increase by decreasing the size of U, and the passband ratio is 113.6 GHz/100 GHz = 1.136.

Figure 10 shows the transmission coefficient of dual-passband FSS with different lengths of S_2 by HIE-FDTD simulation. Due to the change of parameter of S_2, the center frequency of the corresponding passband changes as 112.8, 114.4, and 116.2 GHz, respectively. Similarly, the passband corresponding to the first resonant unit does not change. The passband ratio is 116.2 GHz/100 GHz = 1.162. The parameter S has a greater influence on the passband center frequency than the parameter U with changing the same length.

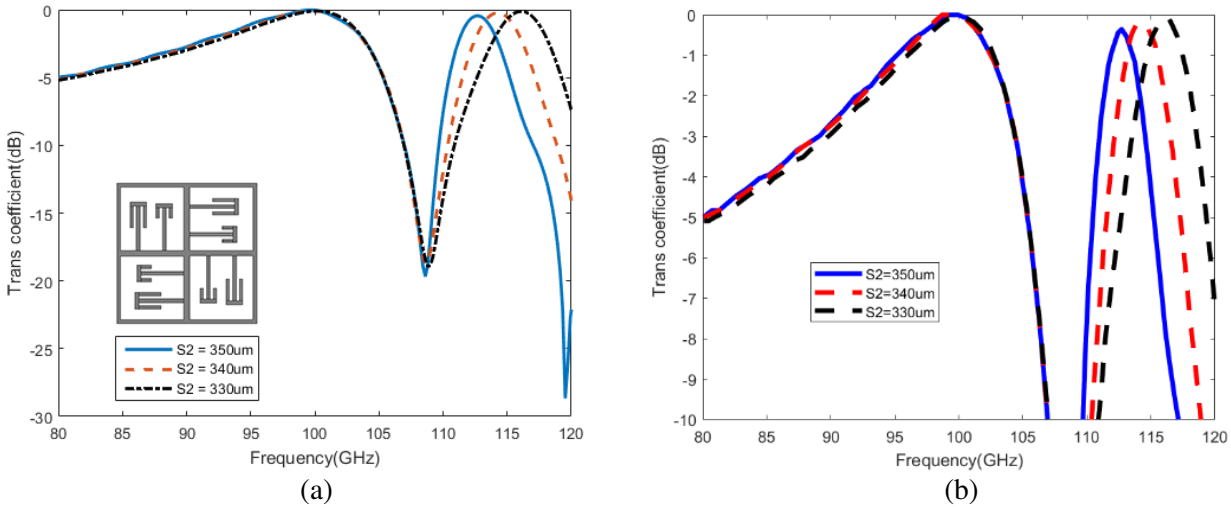

Figure 10. Transmission coefficient of dual-passband FSS with different length of S_2 with different vertical scales: (a) −30 to 0 dB, and (b) −10 to 0 dB ($L_u = 1220\,\mu m$, $D_s = 530\,\mu m$, $T_1 = T_2 = 150\,\mu m$, $S_1 = 350\,\mu m$, $U_1 = 200\,\mu m$, $U_2 = 100\,\mu m$, $W_1 = W_2 = 30\,\mu m$).

Figure 11 shows the transmission coefficient of triple-passband FSS by HIE-FDTD simulation. The size of the first and second resonant units keeps unchanged, and only the size of the third resonant unit is changed. Because of the independence of the passband, it can be found that the passband center frequency corresponding to the first and second resonant units does not change, while the passband center frequency corresponding to the third resonant unit shifts. The passband ratio achieved 222.9 GHz/94.8 GHz = 2.35, which proves that this structure is suitable for designing a millimeter wave multi-passband FSS with high pass band ratio.

Similarly, four-passband FSSs can be achieved by introducing the fourth resonant element into a square slot. Fig. 12 shows the transmission coefficient of four-passband FSSs with different lengths of U_4 by HIE-FDTD simulation, and only the size of the fourth resonant unit is changed. While the other three passband-frequencies remain unchanged, it is only the passband center frequency corresponding to the fourth resonant unit that has deviation, and for three different kinds of four-passband FSSs, this deviated frequency is 249 GHz, 256.1 GHz, and 264.4 GHz, respectively. Comparing the green curve with the orange curve, it can be found that the green curve lacks the second passband because second resonant unit is deleted, while the other three passbands are almost the same as the orange curve. It is proved again that each passband has independent adjustability, which is only related to the corresponding resonant unit. The passband ratio is 264.4 GHz/158.8 GHz = 1.65.

In the proposed structure, the HIE-FDTD simulation results show that each passband of different resonant units is independent. To change the central frequency of a certain passband, only the size of the resonant element in the corresponding square slot needs to be changed. In addition, the structure has good passband adjustment characteristics, which can achieve desired passband ratio, and multi-passband FSSs with large passband center frequency span can be further realized.

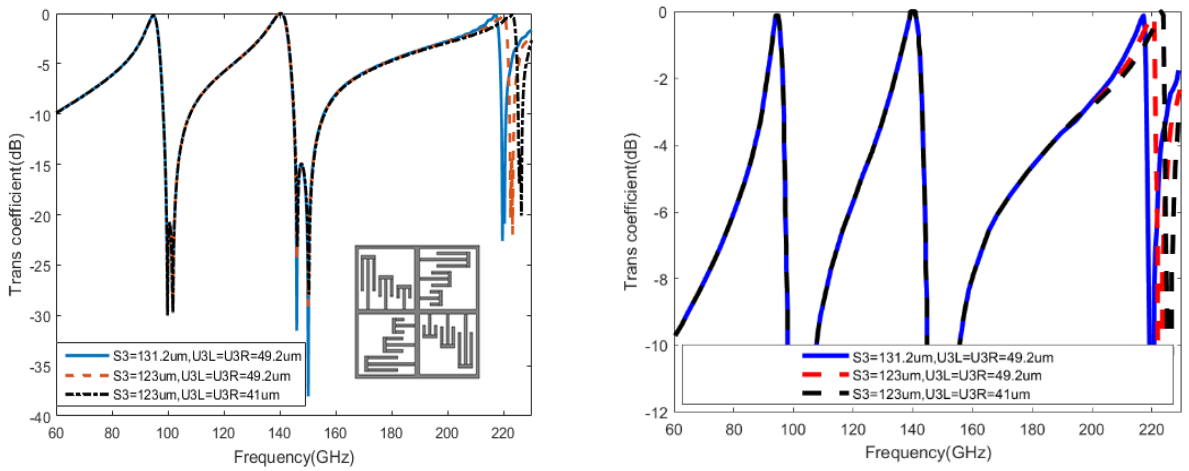

Figure 11. Transmission coefficient of triple-passband FSS with different length of S_3 and U_3 with different vertical scales: (a) -40 to 0 dB, and (b) -10 to 0 dB ($L_u = 1066\,\mu m$, $D_s = 467.4\,\mu m$, $T_1 = T_2 = T_3 = 123\,\mu m$, $W_1 = W_2 = W_3 = 24.6\,\mu m$, $S_1 = 377.2\,\mu m$, $S_2 = 213.2\,\mu m$, $U_1 = 246\,\mu m$, $U_2 = 131.2\,\mu m$).

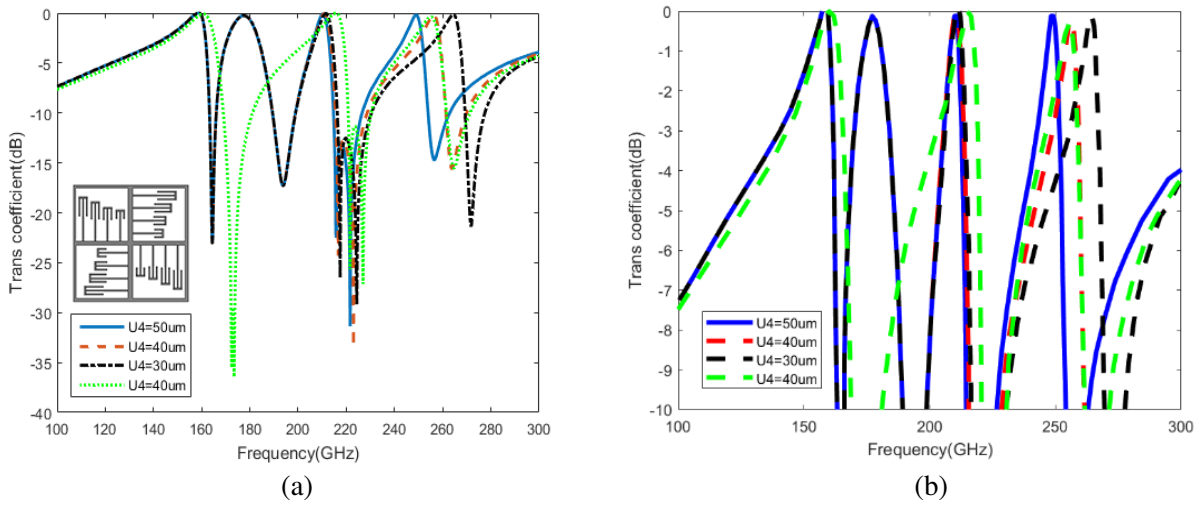

Figure 12. Transmission coefficient of four-passband FSS with different lengths of U_4 with different vertical scales: (a) -40 to 0 dB, and (b) -10 to 0 dB ($L_u = 690\,\mu m$, $D_s = 315\,\mu m$, $T_1 = T_2 = T_3 = T_4 = 60\,\mu m$, $W_1 = W_2 = W_3 = W_4 = 10\,\mu m$, $S_1 = 250\,\mu m$, $S_2 = 205\,\mu m$, $S_3 = 175\,\mu m$, $S_4 = 160\,\mu m$, $U_1 = 125\,\mu m$, $U_2 = 100\,\mu m$, $U_3 = 75\,\mu m$).

4. CONCLUSION

In this paper, cross grove and fork FSS structures in different passbands are designed with the help of HIE-FDTD method. The first FSS structure has good resonance frequency point stability characteristics, and the frequency shift of resonance frequency point is stable within 0.5 GHz at different incident angles. Further, the second FSS structure has good passband adjustability, which can realize desired passband ratio, and even multi-passband FSS with large passband center frequency span. In addition, the self-developed HIE-FDTD algorithm has the characteristic of high accuracy by comparing the measurement and simulation results. This paper provides electromagnetic guides of structure and parameter selections for designing multi-passband FSS.

ACKNOWLEDGMENT

This work was supported by the Zhejiang Provincial Natural Science Foundation of China under Grant No. LQ22F010002, the Scientific Research Foundation of Zhejiang University City College (Nos. J-202218, X-202204 and X-202106), and the Sichuan Science and Technology Program Nos. 2022108 and 2021YJ0087.

REFERENCES

1. Song, X. Y., Z. H. Yan, T. L. Zhang, C. Yang, and R. N. Lian, "Triband frequency-selective surface as subreflector in Ku-, K-, and Ka-bands," *IEEE Antennas Wireless Propag. Lett.*, Vol. 15, 1869–1872, 2016.
2. Salehi, M. and N. Behdad, "A second-order dual X-/Ka-band frequency selective surface," *IEEE Microw. Wireless Compon.*, Vol. 18, No. 12, 785–787, 2008.
3. Deng, R. Y., F. Yang, S. H. Xu, and M. K. Li, "An FSS-backed 20/30-GHz dual-band circularly polarized reflect array with suppressed mutual coupling and enhanced performance," *IEEE Trans. Antennas Propag.*, Vol. 65, No. 2, 926–931, 2017.
4. Deng, R. Y., S. H. Xu, F. Yang, and M. K. Li, "An FSS-backed Ku/Ka quad-band reflectarray antenna for satellite communications," *IEEE Trans. Antennas Propag.*, Vol. 66, No. 8, 4353–4358, 2018.
5. Ma, Y. H., W. W. Wu, Y. Yuan, W. T. Yuan, and N. C. Yuan, "A high-selective frequency selective surface with hybrid unit cells," *IEEE Access*, Vol. 6, 75259–75267, 2018.
6. Zhu, E., Z. Wei, X. Xu, and W.-Y. Yin, "Fourier subspace-based deep learning method for inverse design of frequency selective surface," *IEEE Trans. Antennas Propag.*, IEEE, 2021.
7. Wu, T. K., "Four-band frequency selective surface with double square loop patch elements," *IEEE Trans. Antennas Propag.*, Vol. 42, No. 12, 1659–1663, 1994.
8. Huang, J., T. K. Wu, and S. H. Lee, "Tri-band frequency selective surface with circular ring elements," *IEEE Trans. Antennas Propag.*, Vol. 42, No. 2, 166–175, 1994.
9. Hu, X. D., X. L. Zhou, L. S. Wu, L. Zhou, and W. Y. Yin, "A miniaturized dual-band frequency selective surface (FSS) with closed loop and its complementary pattern," *IEEE Antennas Wireless Propag. Lett.*, Vol. 8, 1374–1377, 2009.
10. Wang, D. S., W. Q. Che, Y. M. Chang, K. S. Chin, and Y. L. Chow, "A low-profile frequency selective surface with controllable tri-band characteristics," *IEEE Antennas Wireless Propag. Lett.*, Vol. 12, 468–471, 2013.
11. Hill, R. A. and B. A. Munk, "The effect of perturbing a frequency selective surface and its relation to the design of a dual-band surface," *IEEE Trans. Antennas Propag.*, Vol. 44, No. 3, 368–374, 1996.
12. Huang, M. J., M. Y. Lv, J. Huang, and Z. Wu, "A new type of combined element multiband frequency selective surface," *IEEE Trans. Antennas Propag.*, Vol. 57, No. 6, 1793–1803, 2009.
13. Chiu, C. N. and W. Y. Wang, "A dual-frequency miniaturized-element FSS with closely located resonances," *IEEE Antennas Wireless Propag. Lett.*, Vol. 12, 163–165, 2013.
14. Romeu, J. and Y. Rahmat-Smaii, "Fractal FSS: A novel dual-band frequency selective surface," *IEEE Trans. Antennas Propag.*, Vol. 48, No. 7, 1097–1105, 2000.
15. Bossard, J. A., D. H. Werner, T. S. Mayer, J. A. Smith, and Y. U. Tang, "The design and fabrication of planar multiband metallodielectric frequency selective surfaces for infrared applications," *IEEE Trans. Antennas Propag.*, Vol. 54, No. 4, 1265–1276, 2006.
16. Li,, B. and Z. Shen, "Dual-band bandpass frequency selective structures with arbitrary band ratios," *IEEE Trans. Antennas Propag.*, Vol. 62, No. 11, 5504–5512, 2014.
17. Miittra, R., C. H. Chan, and T. Cwik, "Techniques for analyzing frequency selective surfaces — A review," *Proc. IEEE*, Vol. 76, No. 12, 1593–1615, 1988.

18. Harms, P., R. Mittra, and W. Ko, "Implementation of the periodic boundary condition in the finite-difference time-domain algorithm for FSS structures," *IEEE Trans. Antennas Propag.*, Vol. 42, No. 9, 1317–1324, 1994.
19. Chen, J. and J. Wang, "A three-dimensional semi-implicit FDTD scheme for calculation of shielding effectiveness of enclosure with thin slots," *IEEE Trans. Electromag. Compat.*, Vol. 49, No. 2, 354–360, 2007.
20. Duan, H., W. Fang, W.-Y. Yin, E. Li, and W. Chen, "Computational investigation of nanoscale semiconductor devices and optoelectronic devices from the electromagnetics and quantum perspectives by the finite difference time domain method," *Progress In Electromagnetics Research*, Vol. 170, 63–78, 2021.
21. Tan, E. L., "Fundamental implicit FDTD schemes for computational electromagnetics and educational mobile apps," *Progress In Electromagnetics Research*, Vol. 168, 39–59, 2020.
22. Tukmakova, A., I. Tkhorzhevskiy, A. Sedinin, A. Asach, A. Novotelnova, N. Kablukova, P. Demchenko, A. Zaitse, D. Zykov, and M. Khodzitsky, "FEM simulation of frequency-selective surface based on thermoelectric Bi-Sb thin films for THz detection," *Photonics*, Vol. 8, No. 4, 2021.
23. Arango, J. D., Y. A. Vélez, V. H. Aristizabal, F. J. Vélez, J. A. Gómez, J. C. Quijano, and J. Herrera-Ramirez, "Numerical study using finite element method for the thermal response of fiber specklegram sensors with changes in the length of the sensing zone," *Computer Optics*, Vol. 45, No. 4, 534–540, 2021.
24. Wang, J. B., J. L. Wang, B. H. Zhou, and C. Gao, "An efficient 3-D HIE-FDTD method with weaker stability condition," *IEEE Trans. Antennas Propag.*, Vol. 64, No. 3, 998–1004, 2016.
25. Hu, T. L., W. Y. Yin, Y. Z. Chen, X. F. Bao, and Z. G. Zhao, "Parallel computing graphene frequency selective surface (GFSS) with large finite array using HIE-FDTD method on high performance computer," *Proce. IEEE ISAPE*, 1–4, 2018.
26. Unno, M., S. Aono, and H. Asai, "GPU-based massively parallel 3-D HIE-FDTD method for high-speed electromagnetic field simulation," *IEEE Trans. Electromag. Compat.*, Vol. 54, No. 4, 912–921, 2012.
27. Huang, B. K., G. Wang, and Y. S. Jiang, "A hybrid implicit explicit FDTD scheme with weakly conditional stability," *Microw. Opt. Technol. Lett.*, Vol. 39, No. 2, 97–101, 2003.
28. Turner, G. M. and C. Christodoulou, "FDTD analysis of phased array antennas," *IEEE Trans. Antennas Propag.*, Vol. 47, No. 4, 661–667, 1999.
29. Guo, C., H. J. Sun, and X. Lu, "Dualband frequency selective surface with double-four-legged loaded slots elements," *2008 International Conference on Microwave and Millimeter Wave Technology*, 2008.
30. Rahmati, B. and H. R. Hassani, "Multiband metallic frequency selective surface with wide range of band ratio," *IEEE Trans. Antennas Propag.*, Vol. 63, No. 8, 3747–3753, 2015.